AIP | Physics of Fluids

Sediment resuspension and erosion by vortex rings

R. J. Munro, N. Bethke, and S. B. Dalziel

Citation: Physics of Fluids **21**, 046601 (2009); doi: 10.1063/1.3083318
View online: http://dx.doi.org/10.1063/1.3083318
View Table of Contents: http://scitation.aip.org/content/aip/journal/pof2/21/4?ver=pdfcov
Published by the AIP Publishing

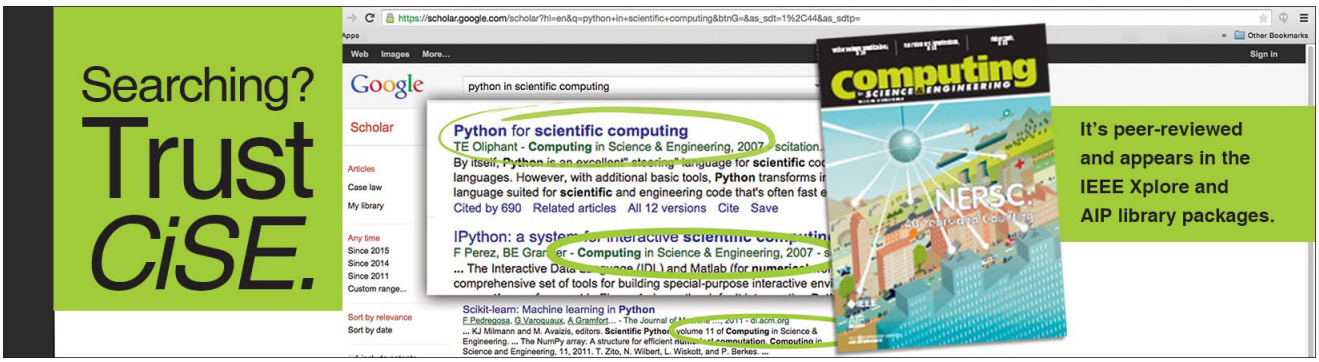

Sediment resuspension and erosion by vortex rings

R. J. Munro,[1,a)] N. Bethke,[2] and S. B. Dalziel[2]
[1]*Environmental Fluid Mechanics Research Group, Process and Environmental Research Division, Faculty of Engineering, University of Nottingham, Nottingham NG7 2RD, United Kingdom*
[2]*Department of Applied Mathematics and Theoretical Physics, University of Cambridge, Cambridge CB3 OWA, United Kingdom*

(Received 17 July 2008; accepted 26 January 2009; published online 8 April 2009)

Particle resuspension and erosion induced by a vortex ring interacting with a sediment layer was investigated experimentally using flow visualization (particle image velocimetry), high-speed video, and a recently developed light attenuation method for measuring displacements in bed level. Near-spherical sediment particles were used throughout with relative densities of 1.2–7 and diameters (d) ranging between 90 and 1600 μm. Attention was focused on initially smooth, horizontal bedforms with the vortex ring aligned to approach the bed vertically. Interaction characteristics were investigated in terms of the dimensionless Shields parameter, defined using the vortex-ring propagation speed. The critical conditions for resuspension (whereby particles are only just resuspended) were determined as a function of particle Reynolds number (based on the particle settling velocity and d). The effects of viscous damping were found to be significant for $d/\delta < 15$, where δ denotes the viscous sublayer thickness. Measurements of bed deformation were obtained during the interaction period, for a range of impact conditions. The (azimuthal) mean crater profile is shown to be generally self-similar during the interaction period, except for the most energetic impacts and larger sediment types. Loss of similarity occurs when the local bed slope approaches the repose limit, leading to collapse. Erosion, deposition, and resuspension volumes are analyzed as a function interaction time, impact condition, and sediment size. © *2009 American Institute of Physics*. [DOI: 10.1063/1.3083318]

I. INTRODUCTION

Particle resuspension and erosion from a layer of negatively buoyant sediment are phenomena of importance in many environmental and industrial processes. Examples include sediment transport in rivers and tidal estuaries, sand drift in deserts, wind-blown snow, reduction in soil fertility due to dust loss from soils, the transport of particulate matter via pipeline systems, and sewage sedimentation tanks (in which the requirement is to prevent resuspension from occurring).

Primarily, sediment resuspension and transport is associated with high Reynolds number flows and turbulence, whereby individual grains are entrained from, or displaced along, a sediment bed as a direct result of the fluid action above it. Early studies of alluvial streams and turbulent channel flows[1–4] established a number of empirical formulations based on careful experimental observations using both natural and artificial sediments, although with limited general validity. However, our understanding of the physics controlling resuspension, transport, and redistribution of sediments, and their relation to turbulent processes, remains weak.

More recent experimental studies have focused attention on the near-wall region of turbulent boundary layers in an open channel flow.[5–11] Using artificial micron-sized sediment (with relative density 1.05), Kaftori *et al.*[7] showed particle transport, resuspension, and deposition to be largely controlled by the action of streamwise coherent wall structures identified as funnel-type vortices (i.e., taking the shape of an expanding spiral, wound around a funnel laid sideways in the direction of the flow). Further experiments,[9] with improved resolution of the fluid flow field and particle motions in the near-wall region, have extended this study to consider natural sediments. These observations showed the flow field to exhibit alternating regions in which low-speed fluid is ejected away from the flow boundary and high-speed fluid injected toward it, the mechanism largely associated with the bursting phenomena responsible for production and maintenance of turbulent boundary layers. Moreover, the turbulent bursting mechanism is believed to be related to the production of sediment-laden kolks and boils observed in rivers.[12]

Sutherland[13] was the first investigator to associate the mechanism of resuspension with coherent structures interacting with the near-surface region of a turbulent boundary layer. Using an isolated vortex ring as a prototypical model, Sutherland speculated that the viscous sublayer is disrupted when an energetic coherent vortex interacts with a sediment layer, leading to an increase in the local shear acting across the near-surface sediment grains. Depending on the submerged weight of the sediment grains and how much of their volume is exposed above the mean bed level, the flow field of the interacting vortex can be sufficient to induce motion, whether it be rolling or saltating of sediment grains along the bed surface, or resuspension.

Despite such advancements, it remains difficult to delineate how a complex, intermittent turbulent flow interacts

a)Author to whom correspondence should be addressed. Electronic mail: rick.munro@nottingham.ac.uk.

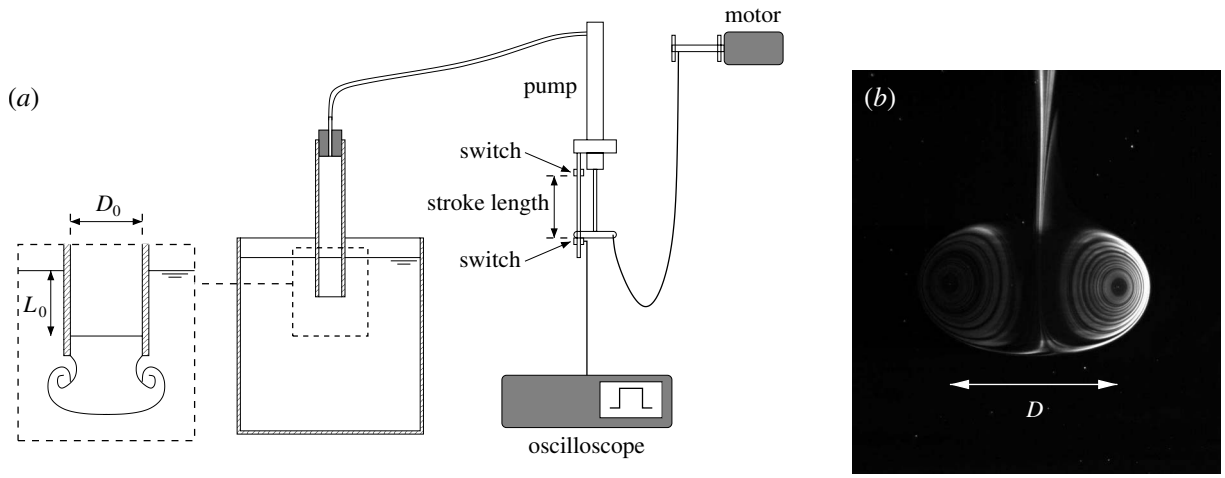

FIG. 1. (a) Schematic showing the system used to generate the vortex rings. The inset shows the slug length L_0, defined as the depth of fluid ejected from the orifice. (b) Image of an illuminated vortex-ring cross section illustrating how the ring diameter D is defined. The ring shown is fully formed with $L_0/D_0=0.9$, $D=4.0$ cm, and $Re=3700$.

with and resuspends sediment. One alternative approach is to consider turbulence as an ensemble of elemental vortex structures and to analyze, in isolation, resuspension by individual vortices. A similar idea has been used in previous studies as a basic model for turbulent entrainment and mixing.[14–16] This approach shall be adopted here. Following Sutherland,[13] we shall consider particle resuspension by vortex rings.

The vortex ring represents one of the simplest vortex structures, which can be easily and consistently produced in the laboratory. Moreover, the dynamics of vortex-ring interaction with solid boundaries is known from previous experimental studies[17] and numerical simulations.[18,19] Of course, this mechanism is notably different from the streamwise funnel vortices[7–9] found in turbulent channel flows, and is more readily associated with turbulence in the absence of a mean flow. Although it has received considerably less attention, resuspension by zero-mean turbulence is of widespread importance in many industrial processes. Previous experimental studies include resuspension by grid-generated turbulence[20,21] and resuspension by jets.[22]

This article describes experimental results regarding the interaction between a vortex ring and sediment layer. Following recent developments in measurement techniques,[23,24] particular focus is given to analyzing levels of sediment erosion and redistribution induced during the period of interaction. Moreover, the flow field of the vortex ring is analyzed in the near-bed region by high-speed time-resolved particle image velocimetry (PIV) and used to determine the critical criteria required to induce incipient resuspension. A range of (artificial) sediment types are used.

II. EXPERIMENT DETAILS

The experiments were performed in a $30\times30\times40$ cm^3 acrylic tank partially filled with tap water. Each vortex ring was generated using a cylindrical tube (internal diameter: $D_0=3.9$ cm) positioned vertically above the center of the tank with the outlet submerged below the water free surface. The inlet of the tube was connected (via an air-tight seal) to a cycle track pump by a length of plastic hose. A schematic side view of the experimental setup is shown in Fig. 1(a). Actuation of the pump expands the air-filled cavity inside the tube, forcing a predetermined volume of water through the outlet, resulting in the rollup and formation of a vortex ring. (Details of vortex ring formation have been widely studied.[25–29])

The characteristics of each vortex ring are determined by the outlet diameter D_0, the stroke time and stroke length of the pump, and the velocity history of the pump mechanism.[29] To facilitate the generation of consistent vortex rings, the actuation rate of the pump was controlled by attaching the pump handle to a motor-driven spindle using a length of nylon cord [see Fig. 1(a)]. A potentiometer controlled the motor speed, with the stroke time of the pump measured using an oscilloscope connected to sensors, located to detect the start and end of the stroke action. A sufficient length of cord was used to ensure that the pump was actuated only when the motor had reached a constant speed. High-speed visualizations of the pump action confirmed that the pump handle moved at a constant speed once the slack cord had been wound up. Stroke lengths of 7 and 20 cm were used throughout, consistently producing fluid slugs with respective lengths $L_0=3.5$ cm and $L_0=10$ cm [i.e., $L_0/D_0=0.9$ and 2.5, respectively, where L_0 and D_0 are shown in Fig. 1(a)].

The characteristics of each vortex ring were determined as a function of the pump stroke time. A set of experiments was performed using fluorescent dye to mark the initial fluid slug, and a thin vertical light sheet to illuminate the midplane of the vortex ring during formation and propagation. A typical cross section of a fully formed vortex ring is shown in Fig. 1(b). The ring trajectories were recorded using a digital video camera, then analyzed to measure the ring diameter D [defined as the diameter of the ring core, as illustrated in Fig. 1(b)], the speed during propagation U, and hence the ring Reynolds number, $Re=\rho UD/\mu$ (where ρ and μ are fluid density and dynamic viscosity, respectively). Each ring was fully formed having moved a distance of order D_0 from the outlet,[25] after which the diameter and the propagation speed

TABLE I. The relevant properties of the particles used. The † symbol denotes those data for which time-dependent measurements were obtained.

Label	Material	ρ_p (g cm^{-3})	d (μm)	w_s (cm s^{-1})	Re_p	α (deg)
A	Glass	2.5	90	1.3	1.2	20
B†	Glass	2.5	150	2.2	3.3	22
C	Glass	2.5	250	3.2	8.0	23
D†	Glass	2.5	350	5.1	17.9	24
E	Glass	2.5	500	7.1	35.5	26
F†	Glass	2.5	700	9.4	65.8	26
G†	Glass	2.5	1000	15.2	152.0	28
H	Diakon	1.2	600	2.4	14.4	24
I	Mustard seed	1.2	1600	4.8	76.8	23
J	Stainless steel	7.0	1100	24.4	268.4	35

remained close to constant until the bottom boundary influenced the motion of the ring when at a height D_0 above the tank base. The ring diameter D and propagation speed U are defined from this period of constant motion. In all experiments, $D \geq D_0$. Empirical formulae relating D and U to the measured pump stroke time were obtained for both cases $L_0/D_0=0.9$ and 2.5. The maximum variation between the measured and empirical values of D and U was, in all cases, less than 5% and 4%, respectively. It has been shown previously[14] that the translational speed of a freely propagating laminar vortex ring in water will decay exponentially (with distance from some virtual origin). In our experiments the propagation distance of the fully formed rings (prior to impact) was restricted to a distance of the order $4D_0$ (approximately 16 cm), in which case the effect of any such decay was negligible, for the range of Re considered.

The resuspension experiments were performed using the apparatus described above with a smooth layer of particles formed across the tank base. Near-spherical particles were used throughout, with a narrow size distribution about a mean diameter. Each particle layer was formed by carefully drawing a flat scraper across the bed surface; the scraper was maintained at a constant height above the tank base by two stainless steel rods (of diameter 1 cm) located along opposing sides of the tank. Excess particles removed during the scraping process were pushed against the tank sidewall, away from the intended impact region. This method produced a close-packed bed of consistent mean depth, although, invariably, the bed was not completely flat. The remaining features had a typical length scale of the order of several centimeters in the transverse plane of the bed, and a depth of order comparable to the particle diameter. We believe that the small amplitude and long wavelength of the initial bedform irregularities did not adversely affect the dynamics of the interaction.

Attention was focused on the case of a vortex ring propagating vertically downwards along the central axis of the tank (so that the ring trajectory was not unduly affected by the tank sidewalls) onto a particle layer of depth 1 cm. This depth ensured that complete erosion of the particle layer did not occur and the solid tank base played no role during the interaction. The basic properties of the particles used are summarized in Table I, where ρ_p, d, and w_s denote, respectively, the particle density, particle diameter, and the terminal settling velocity of a single particle. The particle Reynolds number, Re_p, is defined as

$$Re_p = \rho w_s d/\mu. \tag{1}$$

Estimates for the repose angle, α, are also shown in Table I. Here, α was measured by carefully pouring a fixed volume of particles through a narrow funnel outlet to form a conical pile of sediment on the tank base (below the water surface). This process was repeated several times for each particle type with the repose angle taken to be the external slope of the conical pile produced. The readings for the smaller particle types were found to be more consistent than the larger particles, but in all cases the variability of α was within $\pm 4°$.

Several methods were used to obtain quantitative data during the interaction. Measurements of the vortex ring flow field were obtained using PIV. Small, neutrally buoyant tracer particles were used to seed the water volume, with the midplane of the vortex trajectory illuminated by a narrow, vertical light sheet. The trajectories of the seeding particles were recorded using a high-speed digital camera (a Dantec Nanosense III, with 1280×1024 pixel resolution sampling at 500–1000 Hz), positioned to view horizontally through the tank sidewall. The velocity fields were calculated using PIV techniques found in Digiflow.[30]

Measurements of the layer deformation were obtained using a recently developed light attenuation technique.[24] A digital video camera was positioned to view vertically down onto the sediment layer surface, with the layer illuminated from below by a uniform light source located beneath the tank base. A simple calibration procedure relates the light intensity observed at each point on the layer surface to the corresponding layer depth at that point. Images captured during the impact period were then used to determine the vertical displacement field, henceforth denoted by $\Delta z(x,y,t)$, induced in the bedform about the initial bed level. Here, (x,y,z) denote rectangular coordinates with the z-axis aligned antiparallel to the vertical propagation axis of the vortex ring, with the plane $(x,y,0)$ corresponding to the initial bed level. The light attenuation technique requires the constituent sediment particles to be transparent. Therefore,

the opaque particle types I and J (see Table I) could not be used with this method, and so our analysis of erosion levels was restricted to particle types A–H. The investigation of the critical conditions for resuspension (in subsection A) used all ten particle types.

To satisfactorily resolve the short time scale associated with each impact, image sequences during the interaction period were captured using the high-speed camera (described above) sampling at 500–700 Hz. Figure 9 shows two examples of the measured displacement fields corresponding to the quiescent state once all particle motion had ceased, henceforth denoted by $\Delta z_\infty(x,y)$. Each image pixel corresponds to an area of approximately 0.023 mm^2 on the bed surface. Previous estimates[24] of the error typically associated with this procedure, when measuring small vertical displacements within the particle layer, are less than 10%. The axisymmetric nature of the vortex ring means that the displacement fields are best analyzed in terms of the cylindrical coordinate system (r,θ,z) defined in the usual way with $x=r\cos\theta$ and $y=r\sin\theta$ and the origin located at the center of the impact. In particular, each displacement field was transformed into cylindrical form, $\Delta z(r,\theta,t)$, before being analyzed. The vortex-ring time scale $\tau=D/2U$ will be used throughout Sec. III when describing the data.

III. RESUSPENSION CHARACTERISTICS

Following Shields,[1] sediment resuspension is commonly described in terms of the dimensionless Shields parameter $\theta=\sigma_0/(\rho_p-\rho)gd$, where $\sigma_0=\rho u_f^2$ is the bed shear stress and u_f the friction velocity. For a small, isolated grain located at a horizontal boundary, θ represents the ratio between the force exerted by the flow (in upward or streamwise direction) and the restoring force. Resuspension occurs when the hydrodynamic lift force $F_L\sim\pi\sigma_0 d^2$ exceeds the particle buoyancy $F_B=\pi(\gamma-1)\rho g d^3/6$, whereas motion along the boundary is initiated when the hydrodynamic drag $F_D(\sim F_L)$ exceeds the tangential friction force λF_B (where λ is the contact friction factor). When considering resuspension from a sediment layer, additional forces are involved due to interparticle collisions and cohesion. The upward (or streamwise) force resulting from the momentum transfer when two sediment grains collide scales as[10] $\rho_p\sigma_0 d^2$, whereas cohesive forces are known to be significant for fine sediments only,[31] typically with $d\lesssim 30$ μm, significantly smaller than the particles considered in this article. In the present context, therefore, we expect forces of the form F_L and F_B to remain the dominant terms in the force balance for resuspension. Note that, for small sediments, the shear-induced lift force acting on a sediment grain will cease to act once it has risen a distance comparable to the boundary-layer depth (i.e., once the velocity difference across the grain is small). Hence, any observed rise greater than this will be due primarily to the inertia of the grain and the vertical component of fluid velocity.

For each sediment type there will exist a critical value of θ, denoted by θ_c, at (and above) which resuspension is observed and below which there is no resuspension. This we shall refer to as the critical condition for resuspension. Similarly, the threshold of particle motion marks the limit between incipient particle motion (but not resuspension) and rest. In this article attention is focused upon interactions at and above the resuspension threshold: $\theta/\theta_c\geq 1$.

Before presenting the experimental results we first provide a qualitative description of a typical impact. This will be done using Figs. 2–4 which show three different impacts with $\theta/\theta_c\geq 1$. In Fig. 2, the illuminated cross section of a vortex ring is shown during the period of impact, where $d=350$ μm (type D), $D=5.1$ cm, and $\theta/\theta_c=1.2$. Dimensionless times are included in each frame, with t_1 denoting the time at which the ring cores are located at height $z=D/2$ (after which the ring trajectory is notably affected by the bedform). The impact shown in Fig. 3 illustrates the typical behavior of the resuspended particles; in this case, $d=150$ μm (type B), $D=3.9$ cm, and $\theta/\theta_c=1.7$. Here, the fluid above the layer is illuminated by a light source directed across but above the layer surface, so that sediment grains are visible only when displaced or resuspended above the initial bed level. Again, dimensionless times are shown in each frame. In this case the location of the vortex ring is not visible, so t_0 is used to denote the time at which initial layer deformation is observed. (Note however, it is expected that $t_0\approx t_1$.) Figure 4 shows a sequence of midplane velocity and vorticity measurements obtained during the period of impact, with $d=150$ μm (type B), $D=4.2$ cm, and $\theta/\theta_c=1$. Dimensionless times for each flow field are given in the caption.

Figure 2 illustrates how the structure of the vortex ring is affected by the interaction. Once fully formed, the ring propagates vertically downward with nearly constant speed U and diameter D, until it approaches the bed. When the ring core reaches a height $z=D/2$ above the layer surface (i.e., for $t\geq t_1$) its motion is noticeably affected by the presence of the particle layer. That is, the velocity field induced by the ring's image acts to slow the rate of approach toward the boundary and to increase the ring diameter, stretching the vortex, resulting in an increase in peak vorticity within the core (but with circulation conserved). This is similar to the behavior observed when a vortex ring interacts with a solid boundary.[17] The sequence of white crosses included in Fig. 2(i) shows the trajectory of the vortex core during the interaction.

In addition to the vortex ring being affected by its image in the boundary, the (approximate) no-slip condition on the bed induces vorticity of the opposite sign at the boundary. This vorticity separates and is ejected into the inviscid flow region above as a secondary vortex ring, which then interacts with the original (or primary) vortex ring. (This mechanism has been studied previously[17–19] for the case of a vortex ring interacting with a solid boundary.) The secondary ring, which is not dyed, is first seen in Fig. 2 deforming the outer streamlines of the primary ring at $(t-t_1)/\tau=1.1$. In subsequent frames the secondary ring is clearly visible as dye is entrained within its structure it is advected around the perimeter of the primary. The ejection of the secondary vortex ring from the boundary-layer region causes the primary ring to rebound away from the layer surface; the opposite-sense circulation of the secondary vortex ring [clearly evident in the vorticity maps in Figs. 4(b) and 4(c) acts to slow the outward

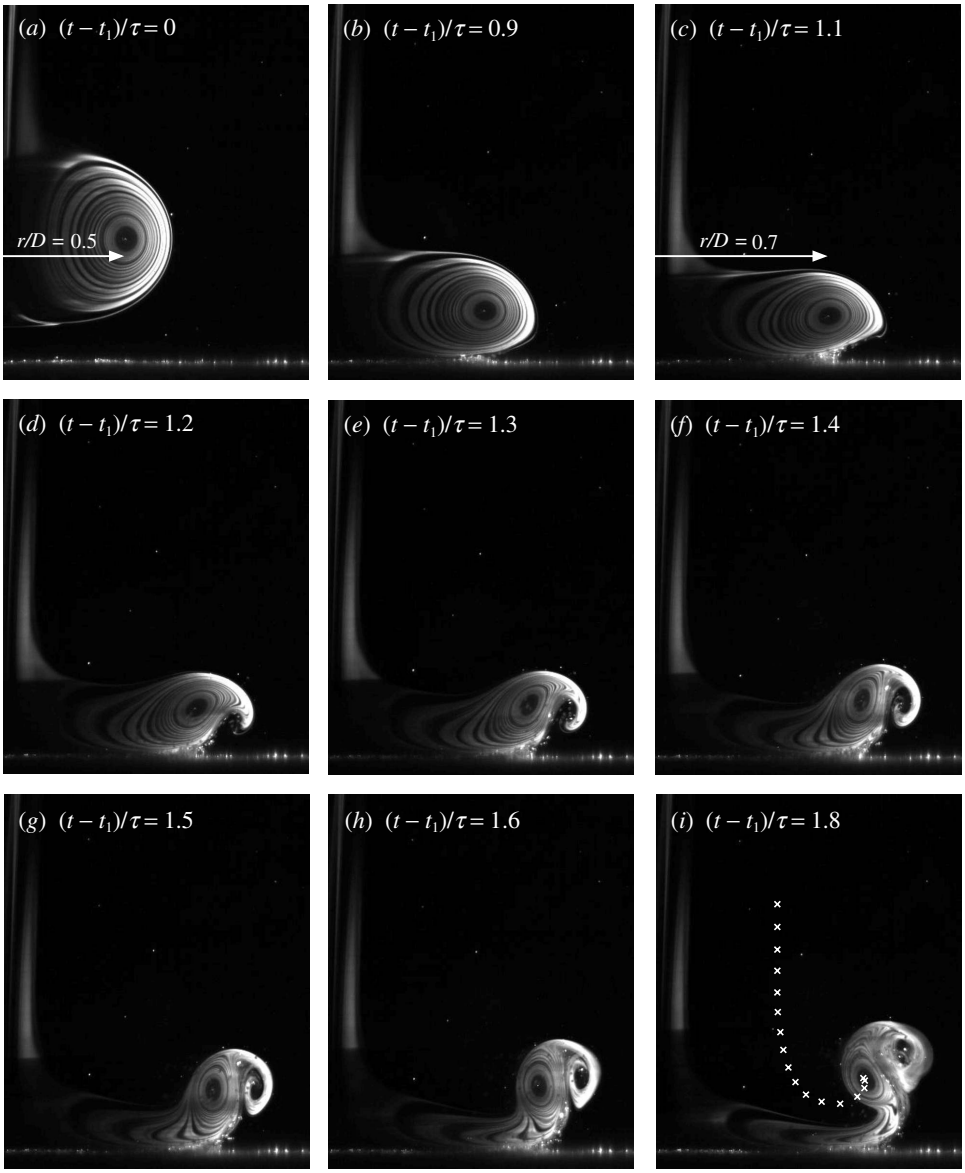

FIG. 2. Image sequence showing the illuminated cross section of a vortex ring during an impact with $d = 350$ μm (type D), $\theta/\theta_c = 1.2$, $Re = 5700$, $D = 5.1$ cm, and $\tau = 0.23$ s. Corresponding dimensionless times are shown, where t_1 denotes the time at which the ring cores are located a height $D/2$ above the layer surface. The series of crosses in frame (i) show the path of the primary-ring core position; the first position corresponds to dimensionless time $(t-t_1)/\tau = -1$, with subsequent positions shown at time steps of 0.175τ.

radial motion of the primary ring. The sequence of white crosses in the final frame of Fig. 2 illustrate the reversal in direction of the (vertical) ring trajectory at approximately $(t-t_1)/\tau = 1.1$.

The bed shear stress was not measured in our experiments. However, $\sigma_0(r,\theta,t)$ will scale with the square of the tangential component of fluid velocity above the layer surface, the typical variation of which is illustrated by Fig. 5. Here, $u_0(r,t)$ denotes the radial component of fluid velocity measured at fixed height $z = 0.1$ cm; the data shown are taken from the velocity measurements in Fig. 4. Predictably, the bed shear stress is maximum directly below the vortex core and increases in magnitude as the vortex is stretched and approaches the bed, reaching its peak value at time $(t-t_1)/\tau = 1.0$ and radius $r/D \approx 0.6$. The subsequent decrease in the magnitude of $u_0(r,t)$ observed in the $(t-t_1)/\tau = 1.1$ profile occurs when the direction of the primary-ring trajectory is reversed by the ejected secondary vortex ring.

Incipient particle motion was consistently observed at $t \approx t_1$ (when the ring core is at a height $z \approx D/2$). Near-surface particles are displaced, primarily, in the region below the ring core where the bed shear stress is maximum, with little if no motion induced below the axial stagnation point or at radii much beyond the instantaneous ring circumference. Initially, the displaced particles slide, roll, or bounce over the undisturbed grains below, eventually forming into a circular mound just beyond the instantaneous ring radius (where the fluid motion is relatively stagnant). The illuminated outline of the particle mound can be seen in Figs. 3(a) and 3(b), whereas Figs. 2(b) and 2(c) show the particles being displaced below the ring core. Moreover, the axisymmetry of the mound structure demonstrates that the particles are displaced, predominantly, along radial trajectories. The mound diameter increases as the vortex is stretched (see Fig. 3) and grows in extent as more particles are displaced.

Resuspended particles become entrained within the outer streamlines of the vortex ring and are advected around the ring perimeter. Passing below the ring core they become subject to a region of positive vertical velocity, which acts to propel them above the layer surface,[13] resulting in a distinc-

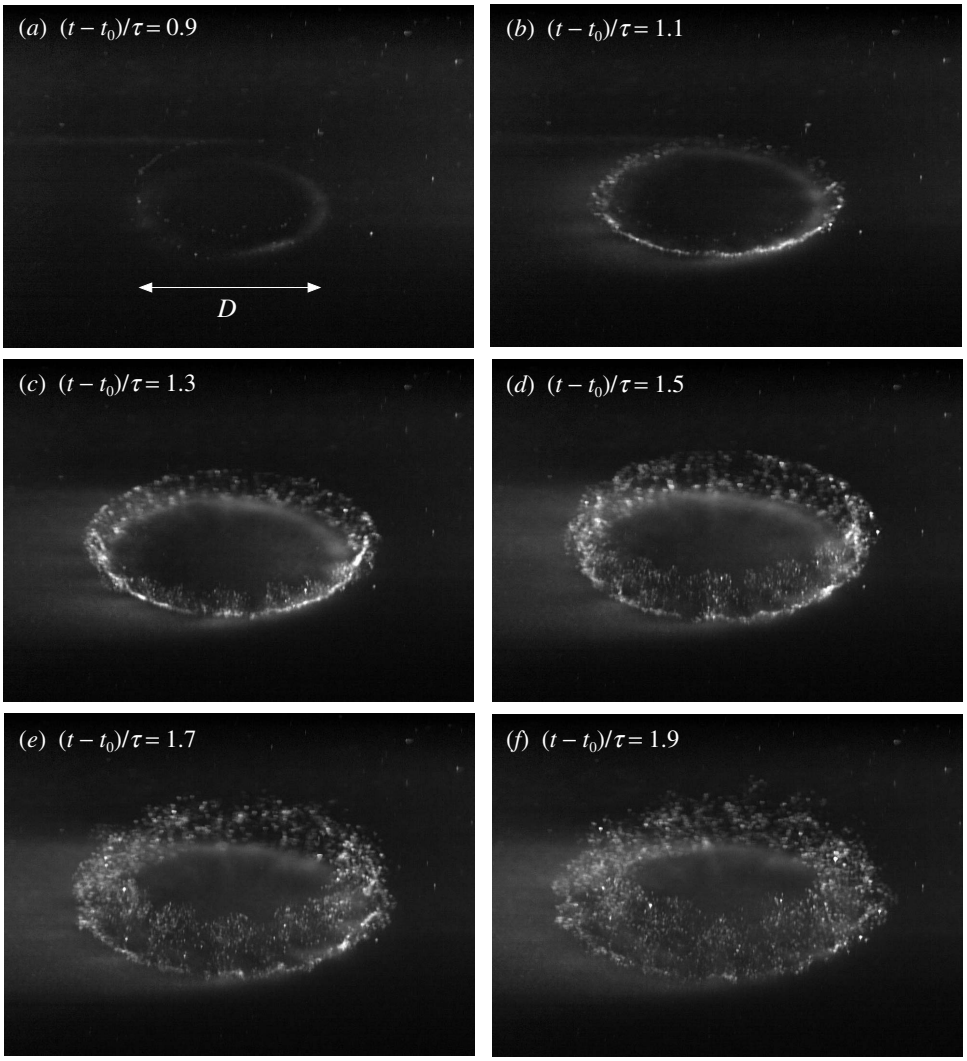

FIG. 3. Sequence of images showing an impact with $d=150$ μm (type B), $\theta/\theta_c=1.7$, $Re=4900$, $D=3.9$ cm, and $\tau=0.16$ s. Dimensionless times are also shown, t_0 denoting the time at which initial bed deformation is observed.

tive splash of resuspended material originating from the mound crest, as shown in Fig. 3. Some of the resuspended grains can also become entrained within the structure of the secondary vortex ring (see Fig. 2). Initial formation of the splash feature was consistently observed at $r/D\approx 0.6-0.7$ and at time $(t-t_1)/\tau\approx 1$, for all particle types and over a range of impact conditions. It is at this radius and time that $u_0(r,t)$ attains its peak value (see Fig. 5). The volume of material resuspended and the height of resuspension, both depend on θ and on the particle properties (ρ_p and d). At $(t-t_0)/\tau\approx 2$, the structure of the vortex ring breaks down, with the impact crater having reached its maximum extent. The characteristic motion scales within the vortex structure continually decrease and become turbulent. With no mechanism to maintain it, the turbulence rapidly decays allowing the resuspended material to settle out of suspension [Fig. 3(f)].

A. Critical conditions for resuspension

The critical conditions for resuspension were found by fixing the properties of the sediment layer while systematically increasing U until resuspension was initiated. This was repeated for each of the ten particle types, with the condition for incipient resuspension taken to be when the particle splash was only just induced by the impact.

As the vortex ring interacts with the sediment bed, a boundary layer is established adjacent to the bed surface. Under critical conditions (and ignoring effects due to bed permeability), we expect[17] the depth of the boundary layer to be approximately $D(\nu/DU_c)^{1/2}=D\,Re^{-1/2}$ and the thickness of the inner viscous sublayer to be $\delta=\nu/U_c=D\,Re^{-1}$. The magnitude of the (tangential) drag and (upward) lift forces acting on the near-surface particles will be dependent on d/δ. That is, if the grain size is large in comparison with the sublayer thickness, the vertical velocity gradient acting across the grain will scale with the outer (inviscid) flow immediately above the boundary-layer region. However, if $d/\delta\lesssim 1$ viscous stresses act to significantly reduce both the fluid velocity and velocity gradient acting on and across the grain, thereby reducing the drag and lift forces. Under critical conditions ($\theta/\theta_c=1$), the measured values of D and Re gave estimates for d/δ between 10 and 290 for the range of sediment types considered. Furthermore, measurements of $u_0(r,t)$, similar to the profiles shown in Fig. 5, were obtained

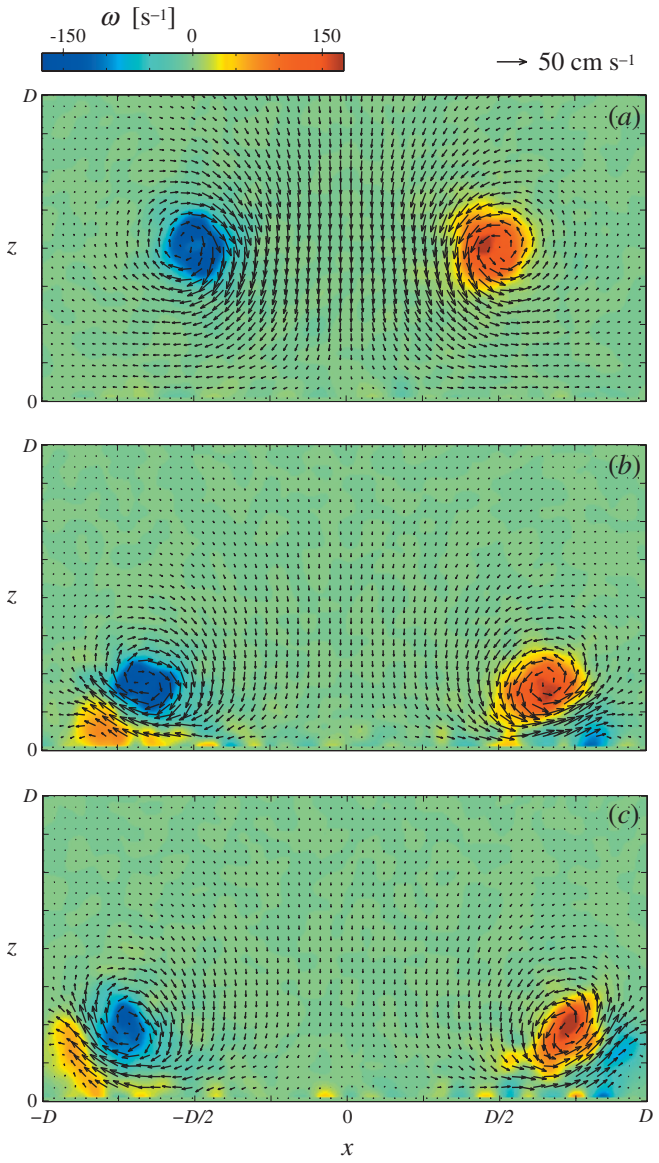

FIG. 4. (Color) Velocity and vorticity measurements from an impact with $d=150$ μm (type B), $\theta/\theta_c=1$, $Re=4000$, and $D=4.2$ cm. The measurements show the midplane of the vortex ring at dimensionless times (a) $(t-t_1)/\tau=0$, (b) $(t-t_1)/\tau=1.0$, and (c) $(t-t_1)/\tau=1.3$, with $\tau=D/2U=0.22$ s. The color scale for the azimuthal vorticity component, ω, is shown across the top of the figure, together with an arrow indicating the corresponding velocity scale.

for each sediment type under critical conditions. If $\hat{u}_0$ denotes the peak value of $u_0(r,t)$ observed during the impact period, it was found that $\hat{u}_0/U=2.0\pm0.4$. Similarly, if $\hat{w}_0$ denotes the peak value of the vertical velocity component (also measured at $z=0.1$ cm), $\hat{w}_0/U=0.6\pm0.2$. In all cases, $\hat{u}_0$ and $\hat{w}_0$ were observed to occur at time $(t-t_0)/\tau\approx1$ and at radius $r/D\approx0.6$–0.7, corresponding to where the resuspension splash is first observed. We therefore expect the peak value of σ_0 to scale with ρU^2 during the impact period. Hence, in the present context, the Shields parameter is defined as

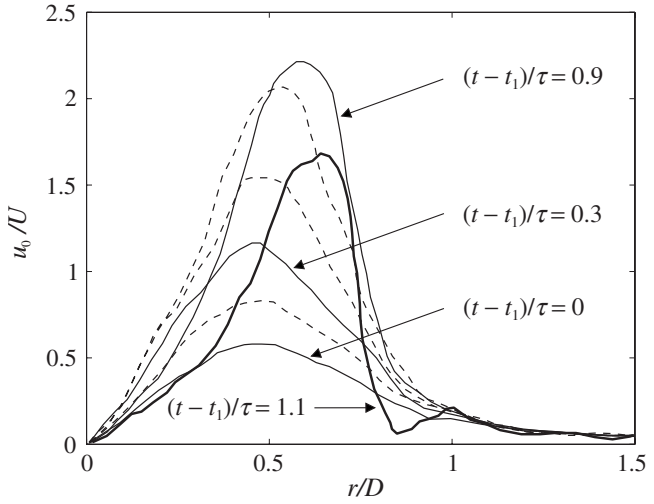

FIG. 5. Measured values of u_0/U plotted against r/D at various dimensionless times. The corresponding times are shown for the solid-line profiles (and indicated by the arrows); the broken lines show profiles at intermediate times: $(t-t_1)/\tau=0.15,0.5,0.7$.

$$\theta=\frac{U^2}{(\gamma-1)gd}, \tag{2}$$

where $\gamma=\rho_p/\rho$ is the relative particle density. The critical-state value of U will henceforth be denoted by U_c.

The critical Shields parameter θ_c was determined by measuring U_c directly from vortex ring velocity measurements. Recall, U_c is the vortex-ring propagation speed measured from the period of steady motion before the ring trajectory is notably affected by the sediment layer. Figure 6 shows the measured values of θ_c plotted against (*a*) Re_p and (*b*) d/δ. For $d/\delta\geq15$, the data are consistent with the $\sigma_0\sim\rho U_c^2$ assumption, whereby θ_c is approximately constant and within the range $1\leq\theta_c\leq2$. That is, in the absence of cohesive and contact forces, the critical condition for resuspension requires that the submerged particle weight $\pi(\gamma-1)\rho gd^3/6$ be exceeded by the inertial lift force $c_\ell\pi\rho U_c^2d^2/4$ acting on the particle, c_ℓ being an $\mathcal{O}(1)$ lift coefficient[3,31] dependent on Re_p. Equating the particle weight to the inertial lift force gives the condition: $\theta_c\sim\mathcal{O}(1)$.

Conversely, the monotonic increase in θ_c observed in our experiments for $d/\delta<15$ indicates that the effects of viscous damping are significant when $d\leq150$ μm, in agreement with earlier results of White,[32] who suggests the appropriate critical grain size to be $d\leq200$ μm (for an impact under critical conditions). It is also worth noting that as the grain size d becomes comparable to the thickness of the viscous sublayer $(d/\delta\sim1)$, the inertial lift force acting on a surface grain[33] will be $\mathcal{O}(\rho U_c^4d^4/\nu^2)$. The corresponding critical resuspension condition in this case reduces to $\theta_c\sim Re_p^{-1/2}$, where it is assumed that terminal settling velocity of an isolated grain is given by $w_s=(\gamma-1)gd^2/18\nu$ (which is valid for $Re_p\ll1$).

The overall trend of the data shown in Fig. 6(a) is similar to that of earlier work[33] on resuspension due to the vortex shed when a solid sphere in free fall collides with a sediment layer. Using various sediment types with grain sizes in the

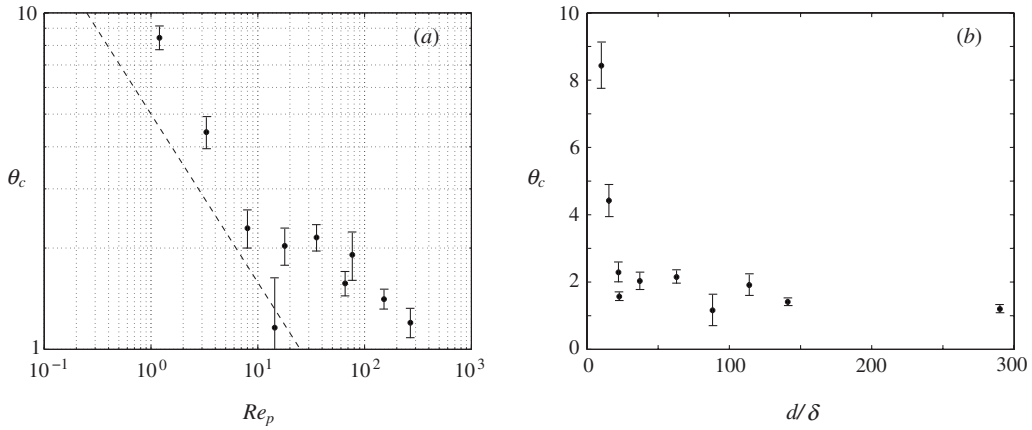

FIG. 6. Measured values of the θ_c plotted against (a) Re_p and (b) d/δ, for each of the particle types shown in Table I. The broken line in (a) shows the curve $\theta_c=5.0\,Re_p^{-1/2}$. The error bars show the variability in the measured values of U_c (typically 3%–6%), based on near-identical repeats (between 4 and 6) of the same experiment.

range 4.5–2000 μm, a semiempirical fit $\theta_c=5.0\,Re_p^{-1/2}$ was found[33] for the $d/\delta\sim 1$ limit; this curve has been included in Fig. 6(a) for comparison (shown as the broken line). The level of scatter evident in Fig. 6 can be attributed to the difficulties associated with observing the precise critical conditions for resuspension, which will depend, although weakly, on the configuration of the individual grains within the sediment layer. In an attempt to minimize this effect, each data point represents an average taken from a number of repeats of the same nominally identical experiment, with the sediment layer reformed between each experiment. Error bars have been included in Fig. 6 to give an idea of the typical variability in the corresponding measured values of U_c.

It should be noted that the two simplified conditions described above are expected to underestimate the actual critical Shields parameter criteria, as neither condition takes account of shielding effects due to neighboring particles. Furthermore, the particles are assumed to be cohesionless throughout. Of course, in the limit as d gets ever smaller, cohesive forces are eventually dominant in comparison with the relative particle weight, and would need to be accounted for. It has been suggested[31] that this situation occurs for very fine dust grains with $d\lesssim 30$ μm, significantly smaller than the particles considered here.

Finally, it should be noted that the values of θ_c shown in Fig. 6(a) are an order of magnitude larger than the traditional values presented in, for example, White[32] and Brownlie.[34] Such estimates are typically based on thresholds of sediment displacement (or resuspension) in a steady turbulent channel flow, in which case the mean velocity profile is well understood and the estimation of u_f is standard (e.g., White[32] uses $u_f=\sqrt{gH\beta}$, where H and β are the channel depth and bed slope, respectively). This is not the case for the experiments described in this article. Here, the boundary layer induced by the interacting vortex ring evolves spatially and with time, and the mean velocity profile within this region is not known. Consequently, a standard estimation of u_f using an analogous procedure was not possible, and θ was therefore defined in terms of characteristic (inviscid) flow speed U.

B. Crater characteristics

We now analyze how the particle layer is eroded by the vortex flow field during the period of impact. Figure 7 shows an impact from the plan view, with $d=150$ μm (type B) and $\theta/\theta_c=6.2$. Figure 8 shows the corresponding stages of a different impact with $d=350$ μm (type D) and $\theta/\theta_c=5.4$. In both cases, $Re=11\,800$ with $D=5.0$ cm. Dimensionless times are included; as before, t_0 denotes the time at which bed deformation is first observed. The features described earlier in this section are readily identified in both image sequences. In particular, near-surface particles are displaced in the region of maximum shear stress directly below the ring core, resulting in the formation of a circular mound, the radius of which increases as the vortex is stretched. The particle splash is initially observed at $(t-t_0)/\tau\approx 1$, while the particle mound reaches its maximum radius at $(t-t_0)/\tau\approx 2$, after which the structure of the vortex ring breaks down into turbulence.

This plan-view perspective shows the spokelike scar features that can form on the crater interior, caused by an azimuthal instability (in the form of a sinusoidal perturbation of the ring core) that develops as the vortex propagates through the fluid.[35,28] Whether or not the instability is observed depends on the Reynolds number Re and on the distance traveled by the vortex. Larger values of either quantity suggest the onset of instability,[35] with the perturbation wavenumber increasing with Re. The likely cause of this perturbation[28] is that vorticity of opposite sign generated inside the orifice as the fluid slug is ejected. This secondary vorticity is then entrained within the vortex core during the rollup process.

The wavelike nature of the instability exposes the crater surface to both radial and azimuthal velocities, the azimuthal component changing direction either side of the amplitude extremum. When $\theta/\theta_c>1$, the instability leads to a more complicated pattern of separation. In some regions the near-surface grains are displaced primarily in the azimuthal direction, forming the spokelike mounds observed. If θ/θ_c is sufficiently large, particles are also observed to be resuspended from the crests of the radial mounds. The scarring pattern

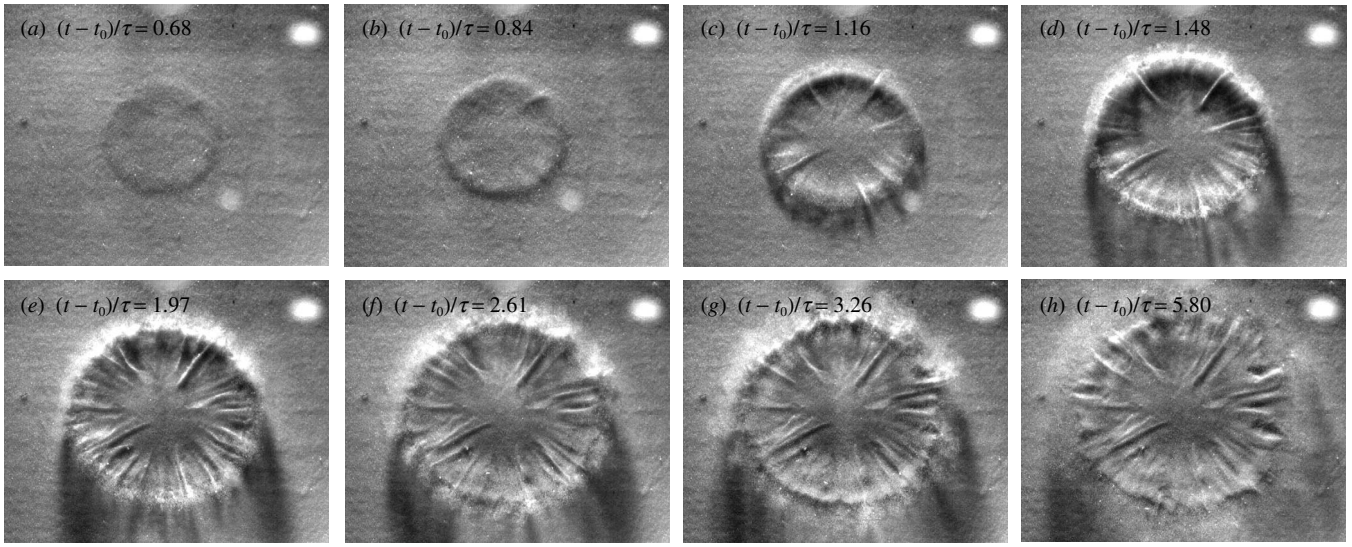

FIG. 7. Sequence of images showing an impact with $d=150$ μm (type B), $\theta=\theta_c=6.2$ $D=5.0$ cm, $\tau=0.106$ s, and $Re=11\,800$. Corresponding dimensionless times are included at the top of each frame. The images were taken viewing down onto the bed surface at an angle of approximately 10° to the vertical, illuminated by a light source directed across the layer surface.

depends on the internal structure of the instability and the small-scale bed constitution, so is different for each impact. An estimate of the instability wavenumber can be obtained by counting the number of radial mounds. For the two impacts shown in Figs. 7 and 8 the wavenumber appears to be between 10 and 12, which is consistent with previous stability analysis[35] for this value of Re. The wavenumber of the banding was observed to increase with Re.

Measurements of the bedform deformation (in terms of vertical displacements about the initial bed surface) were obtained using the light attenuation technique outlined in Sec. II. Figure 9 shows two examples of final-state displacement fields $\Delta z_\infty(x,y)$, corresponding to the quiescent state once all particle motion has ceased. In both cases, a sequence of dynamic measurements $\Delta z(x,y,t)$ (sampled at 500 Hz) was also obtained during the period of impact, as the crater structure is forming. The experiments shown in Figs. 7 and 9(a) were performed independently, although under near-identical conditions. On comparing the displacement map with the final frame of the image sequence, there are notable differences in the small-scale scarring pattern. However, the large-scale displacement structure we expect to be directly comparable. Likewise, the impacts shown in Figs. 8 and 9(b) are from separate experiments performed under near-identical conditions.

The displacement fields are best analyzed when transformed into cylindrical coordinates (r,θ,z). In particular, the (azimuthal) mean crater profile, henceforth denoted $h(r,t)$, is then defined by

$$h(r,t)=\frac{1}{2\pi}\int_0^{2\pi}\Delta z(r,\theta,t)\mathrm{d}\theta. \tag{3}$$

Similarly, $h_\infty(r)$ denotes the mean profile obtained from the final-state craters. The sequences of $h(r,t)$ shown in Fig. 10 demonstrate the typical evolution of the crater structure observed during the period of interaction. Dimensionless times are given for each of the solid-line profiles, with intermediate times indicated by the broken lines (see caption for details). The two sequences shown correspond to the experiments in Fig. 9. It should be noted that the asymmetric (azimuthal) variations on the crater surface, once developed, can affect the structure of the mean profiles $h(r,t)$. In particular, the irregular wavelike outline of the particle mound observed in Fig. 9(b), when averaged, produces the shallow plateau at the rear of the main particle mound that appears in final profile of Fig. 10(b). The same effect in the final profile of Fig. 10(a) is observed as a broadening of the mound structure. For the two impacts shown in Fig. 10, the typical root-mean-square variation between $\Delta z_\infty(r,\theta)$ and $h_\infty(r)$ was found to be (a) $0.0021D$ ($\approx 0.7d$), and (b) $0.0035D$ ($\approx 0.5d$), where, in both cases, $D=5$ cm.

The initial formation of the particle mound occurs at $r/D\approx 0.6$, in the region just beyond where the bed shear stress is maximum (below the ring core). Subsequently, the mound is swept radially outward with the core as the vortex ring is stretched, growing in volume as more particles are displaced. In the region directly below the axial stagnation point of the vortex ring, the bed shear stress is subcritical (i.e., does not induce particle motion), resulting in a mound of uneroded particles remaining at the crater center. (This was not the case for all impacts considered, as will be demonstrated below.) Moreover, in the two impacts shown, at no time does the slope of the crater sidewalls reach the angle of repose; here, the repose angles were measured to be 22° and 24°, respectively (see Table I). A reference angle is included in each sequence to illustrate the local crater slopes. No further erosion of the particle layer occurs beyond $(t-t_0)/\tau \approx 2$ (the time at which the structure of the vortex ring breaks down).

The level of bed erosion is also dependent on the constituent grain size. This is best illustrated by Fig. 11 which compares a set of final-state mean profiles $h_\infty(r)$ for a range

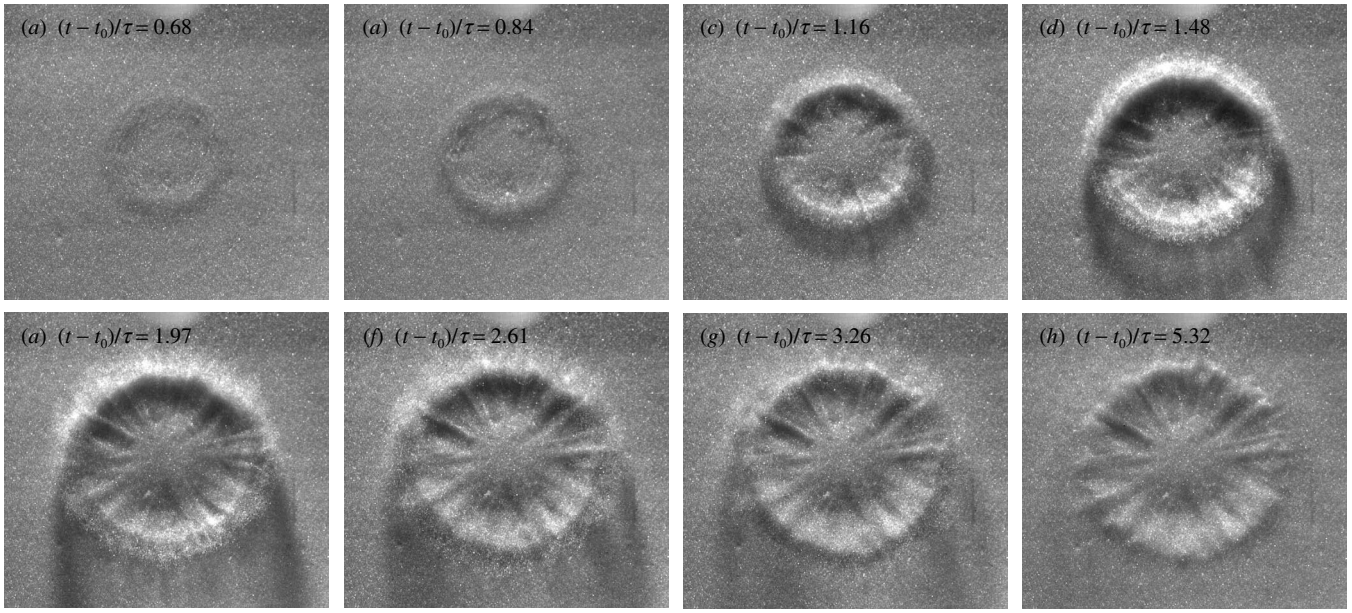

FIG. 8. As for Fig. 7 but with $d=350$ μm (type D), $\theta/\theta_c=5.4$ $D=5.0$ cm, $\tau=0.106$ s, and $Re=11\,800$.

of particle types and for two distinct impact conditions: $\theta/\theta_c=2.3$ and 6.3. Consider first the five profiles (in each plot) corresponding to the particle types B–G with $\gamma=2.5$. For the larger particle types F and G (with $d=700$ and 1000 μm, respectively), the eroded volumes are comparable. However, as the grain size is reduced a corresponding decrease in erosion level is observed. Moreover, the greater penetration of the vortex ring for the larger particle types means that, provided θ is sufficiently large, the slope of the interior crater sidewall reaches angle of repose. The repose angles for particle types F and G are 26° and 28°, respectively; a reference angle of 25° has been included in Fig. 11 for comparison. Even for the less-energetic $\theta/\theta_c=2.3$ impact, the crater slope for the larger particle types F and G approaches an angle close to that of repose.

The relative density of the constituent particles also significantly affects the erosion level. Figure 11 includes two crater profiles for bedforms consisting of the much lower density type-H particles (with $\gamma=1.2$, $d=600$ μm), which are best compared with the corresponding profiles for the particle types E and F (with $\gamma=2.5$ and respective grain sizes $d=500$ and 700 μm). In both impacts, the vortex ring is observed to penetrate much further into the bedform consisting of the lighter sediment. It should be noted, however, that the basic interaction characteristics for these two impacts are essentially the same as those described previously. Also note that for the larger particle types F, G, and H, significant erosion of the bedform is observed at the axial region $r=0$ for the $\theta/\theta_c=6.3$ impact [Fig. 11(b)], but not for the less-energetic $\theta/\theta_c=2.3$ impact. This axial erosion, associated

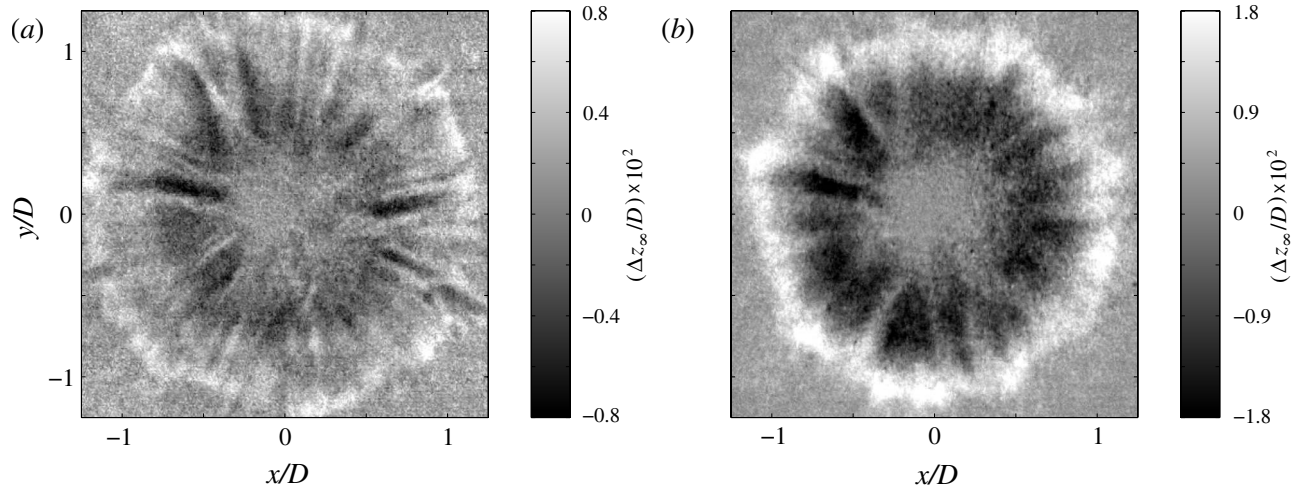

FIG. 9. Final state displacement maps obtained using the light attenuation technique. The two impacts shown correspond to (a) $\theta/\theta_c=6.2$ with $d=150$ μm (type B), and (b) $\theta/\theta_c=5.4$ with $d=350$ μm (type D). In both cases, $Re=11\,800$, $\tau=0.106$ s, and $D=5.0$ cm. These displacement fields can be compared to the respective image sequences shown in Figs. 7 and 8 (although the corresponding experiments were performed independently).

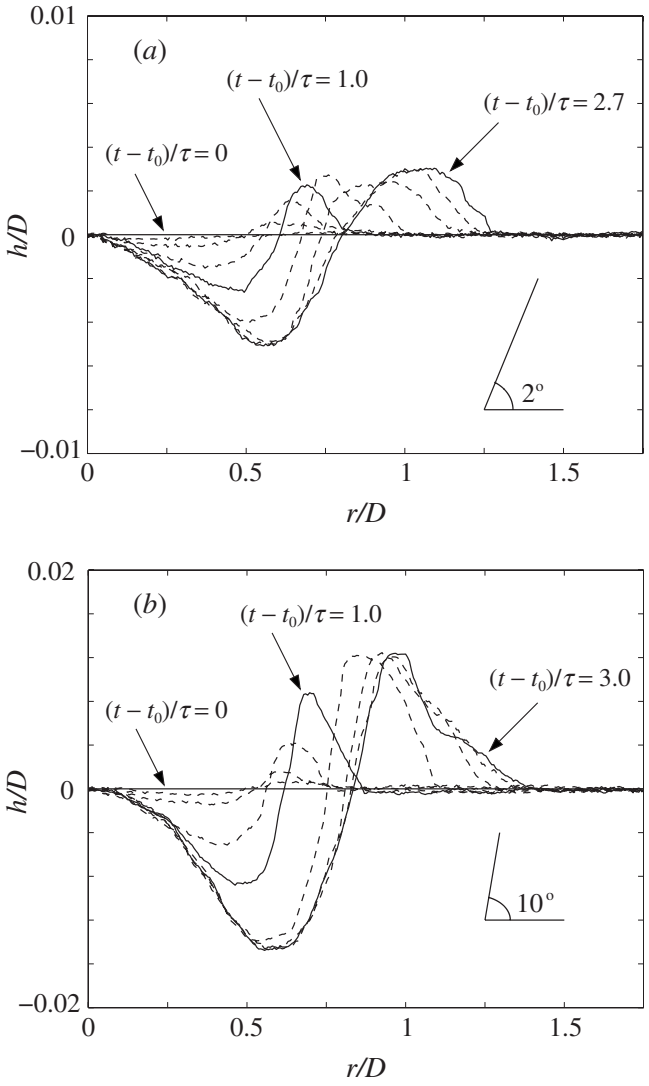

FIG. 10. $h(r,t)$ plotted against r/D at various times during impact. The impact conditions are (*a*) $\theta/\theta_c=6.2$ with $d=150$ μm (type B), and (*b*) $\theta/\theta_c=5.4$ with $d=350$ μm (type D). The data shown are taken from the experiments in Fig. 14. In both cases, $Re=11\,800$, $D=5.0$ cm, and $\tau=0.106$ s. Dimensionless times for the solid-line profiles are shown; the broken-line profiles indicate intermediate times. For $(t-t_0)/\tau \leq 1$ the time step between profiles is approximately 0.25τ (both plots); at later times the time steps are approximately (a) 0.43τ and (b) 0.5τ. The repose angles for these two particle types are (a) 22° and (b) 24°; reference angles are included to illustrate the local bed slope.

with the local crater slope reaching the repose angle and becoming unstable, is consistently observed to occur during the initial stages of the impact within the period $(t-t_0)/\tau \leq 0.8$, before the resuspension splash is observed. We shall return to this point shortly.

The overall characteristics of the eroded sediment layer have been shown to be similar throughout the interaction, for different impact strengths and particle types. To assess the similarity of the crater features during the impact period, the time evolution of a crater profile is plotted again, but now normalized to enable the comparison at different times. The vertical coordinate is normalized by, $|h_0(t)|$, where $h_0(t)$ denotes the instantaneous maximum crater depth, and the radial coordinate is scaled by the instantaneous extent of the eroded region, $R(t)$. Although somewhat arbitrary, these rescalings are chosen as the points of maximum erosion and the crater radius are readily identified for each crater. Figure 12(a) shows the collapse of the crater profiles for the impact with $d=350$ μm (type D) and $\theta/\theta_c=5.4$, as it evolves with time. Note, these are the same data shown in Fig. 10(b). At the earliest times, $|h_0|$ is very small and serves to amplify the signal noise; we have therefore excluded the earliest times from our comparison. However, by $(t-t_0)/\tau=0.3$, the amplification and hence noise level are sufficiently low to demonstrate the near self-similarity of the crater evolution.

The profile collapse indicates that the governing physical mechanisms responsible for the deformation of the particle layer—bedload transport and resuspension—remain similar throughout the interaction. A corresponding degree of collapse is found for individual impacts on bedforms consisting of other particle types and over a range of impact conditions. It is therefore interesting to see whether the bed profiles are also self-similar with variations in the Shields parameter. To this end, the normalized final crater shapes for different values of θ/θ_c (for particle type D, $d=350$ μm) are plotted in Fig. 12(b). In the depositing region, $h(r,t)>0$, Fig. 12(b) shows a strong similarity across a range of θ/θ_c. In the erosion region, the comparison is still good for the three lower values of θ, suggesting a strong similarity in dynamics, but for the highest value of θ the crater shape is clearly different for $r/R<1$. To understand this difference we must consider the mechanism by which the bed has been deformed near $r=0$ in this $\theta/\theta_c=7.7$ case.

Up until now we have concentrated on the role of shear in moving the particles. However, as the impacting vortex ring is axisymmetric with negligible swirl, we expect the shear at the bed to vanish toward the axis (apart from turbulent fluctuations). While there is no radial velocity along the axis of the vortex ring, there is a strong axial velocity. To the leading order approximation, this axial velocity must vanish at the bed, forming a stagnation point at which the pressure increases with the square of the impact velocity. The associated force must be supported by the particle bed, something it is able to do at low θ. However, as θ increases, the bed profile gets steeper and so less able to support the stagnation pressure. We therefore speculate that the point is eventually reached, somewhere between $\theta/\theta_c=5.5$ and $\theta/\theta_c=7.7$, where the central mound begins to collapse. Note that, due to the added load associated with the stagnation pressure, the collapse first occurs when the slope on the inner wall of the crater is still significantly less than the angle of repose. The additional mechanism involved qualitatively changes the shape of the crater and so self-similarity is lost.

A similar picture occurs with the other particle types. For weak rings, the crater shape is self-similar, while for sufficiently strong rings the central mound collapses and self-similarity is lost. The point at which this transition occurs depends on the particle type. As we have seen, deeper craters with steeper sidewalls are formed for the same θ/θ_c with the $d=700$ and 1000 μm particles. This means that stability of the central mound will be lost with a smaller stagnation pressure (and hence smaller impact velocity) than for the $d=350$ μm particles, a feature born out by our observations.

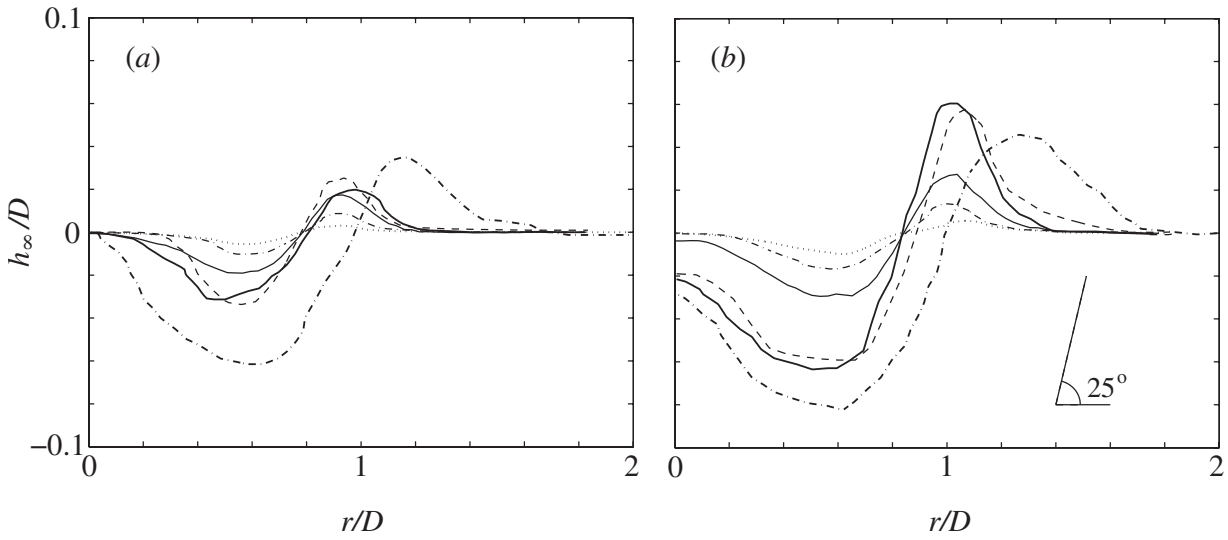

FIG. 11. A comparison of final-state mean profiles, $h_\infty(r)$, for two distinct impact conditions: (a) $\theta/\theta_c=2.3$ and (b) $\theta/\theta_c=6.3$. The six line types indicate the different particle types: B (dotted, $d=150$ μm), D (dotted-dashed, $d=350$ μm), E (solid, $d=500$ μm), F (dashed, $d=700$ μm), G (thick solid, $d=1000$ μm), and H (thick dot-dashed, $d=600$ μm). The repose angle of the particle types shown ranges between 22° and 28°; a reference angle of 25° has been included for comparison.

The ability for $R(t)$ to collapse the developing structure of the erosion process is further illustrated by Fig. 13(a) which compares the temporal development of $R(t)$ for particle types B, D, F, and G over a range of θ/θ_c. By scaling $R(t)$ with its final value R_∞, and $t-t_0$ by a time scale related to the period over which erosion occurs (denoted by τ_e), we see all the impacts follow a similar evolution. The erosion time scale, here defined as the time to reach $R/R_\infty=0.8$, depends on the Shields parameter as well as the vortex ring time scale τ. Although there is some scatter, Fig. 13(b) demonstrates clearly that τ_e/τ increases with θ/θ_c. This is to be expected as a strong vortex ring will start moving particles while still positioned at a greater distance z/D above the bed, and continue to be sufficiently strong enough to do so for more turnover times following the impact.

Figure 14 shows estimates of the eroded volume $V_e(t)$ plotted with deposited volume $V_d(t)$ against dimensionless time; again, these data are taken from the two experiments shown in Fig. 10. The eroded and deposited volumes are defined, respectively, by

$$V_e(t) = 2\pi \int_0^\infty h_e(r,t) r \, dr, \tag{4}$$

$$V_d(t) = 2\pi \int_0^\infty h_d(r,t) r \, dr, \tag{5}$$

where $h_e(r,t)$ and $h_d(r,t)$ denote the negative and positive parts of $h(r,t)$. We estimate the error associated with the measured values of $V_e(t)$ and $V_d(t)$ shown in Fig. 14 to be

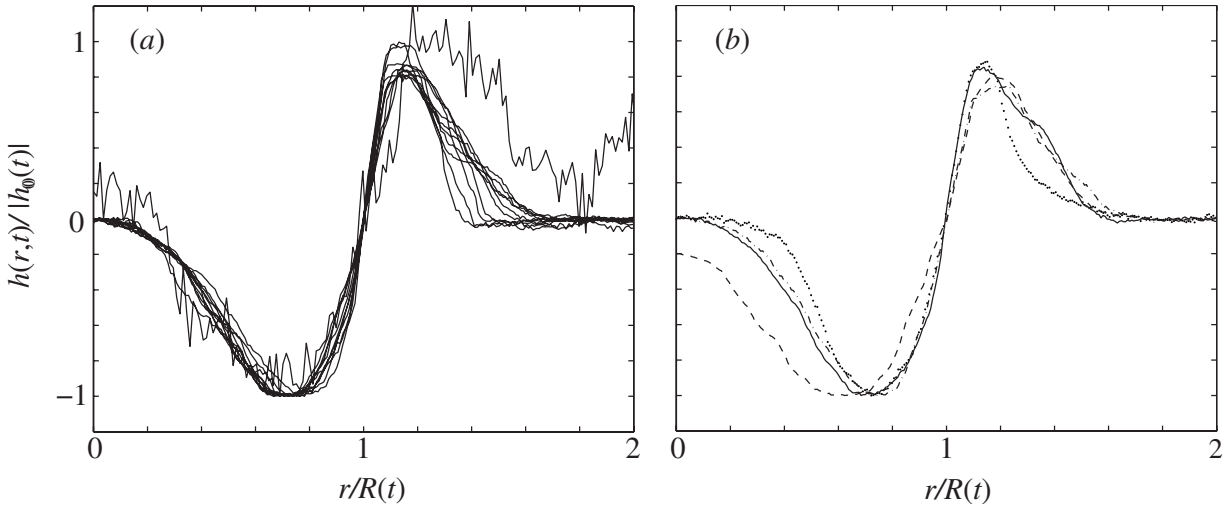

FIG. 12. (a) Plot showing the similarity of the crater profiles during the impact period (for $d=350$ μm, $\theta/\theta_c=5.4$). Profiles between the times $(t-t_0)/\tau=0.3$ to 3.2 are plotted, at discrete 0.25τ intervals. (b) Plot showing the level of similarity for four different impacts: $\theta/\theta_c=2.4$ (dotted), 3.8 (dashed-dotted), 5.4 (solid), and 7.7 (broken). The profiles shown were obtained at time $(t-t_0)/\tau=2$ (corresponding to the final-state profile). In both cases, $h(r,t)$ and r are normalized, respectively, by the instantaneous maximum crater depth $|h_0(t)|$ and the crater radius $R(t)$.

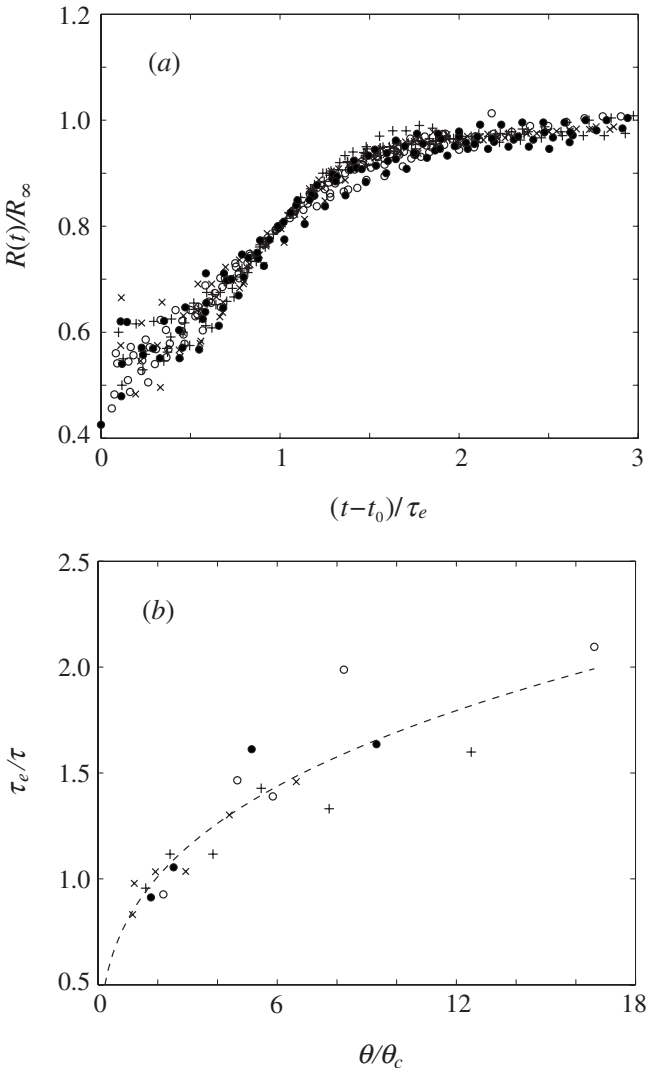

FIG. 13. Plot (a) shows the development of the rescaled crater radius $R(t)/R_\infty$ as a function of dimensionless time. The dependence of the timescale τ_e on θ/θ_c is shown in plot (b). In both cases, the different symbols correspond to particle types B (○, $d=150$ μm), D (+, $d=350$ μm), F (×, $d=700$ μm), and G (●, $d=1000$ μm). The broken line in (b) shows the best-fit curve $\tau_e/\tau=k(\theta/\theta_c)^m$, with $k=0.81$ and $m=0.32$.

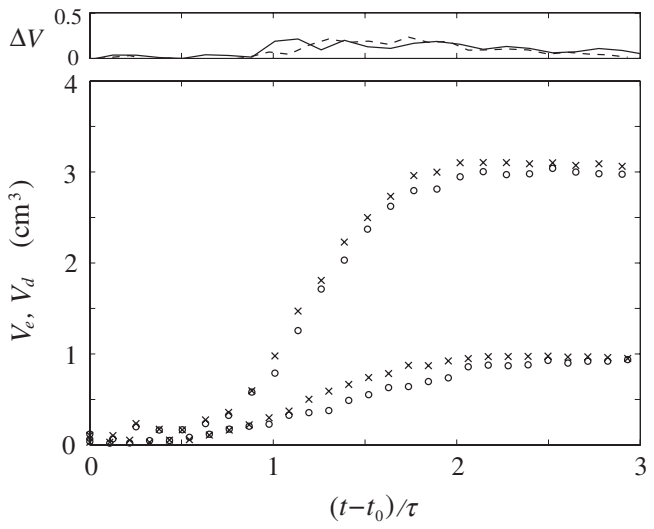

FIG. 14. Eroded volume, $V_e(t)$ (×), and deposited volume, $V_d(t)$ (○), plotted against dimensionless time $(t-t_0)/\tau$. The larger erosion and deposit levels correspond to the experiment shown in Fig. 10(b) (with $d=350$ μm and $\theta/\theta_c=5.4$); the smaller erosion and deposit levels correspond to the experiment shown in Fig. 10(a) (with $d=150$ μm and $\theta/\theta_c=6.2$). The instantaneous volume difference $\Delta V=V_e-V_d$ is plotted across the top of the main plot (with the solid line showing the $d=350$ μm case, the broken line corresponding to $d=150$ μm).

less than 12%, at each time step. Included at the top of Fig. 14 is the corresponding volume difference $\Delta V=V_e-V_d$. Clearly, sediment volume is conserved until $(t-t_0)/\tau\approx 1$, at which point particles become resuspended within the fluid. After this time, the increase in ΔV observed provides an estimate for the instantaneous volume of resuspended material. For $(t-t_0)/\tau\gtrsim 3$, the resuspended volume has fallen out of suspension and returned to the layer surface, after which $\Delta V\approx 0$ once more (certainly to within the inherent noise levels associated with the light attenuation method).

Figure 15 shows the maximum volume difference, denoted by ΔV_0, during the period of resuspension, plotted against θ/θ_c for a range of impact conditions and particle types (all with relative density $\gamma=\rho_p/\rho=2.5$). ΔV_0 has been made dimensionless using the sphere volume $\pi D^3/6$ as an estimate for the ring volume. The data show there to be a clear increase in resuspended volume with θ/θ_c and as d is increased. Of course, the individual particle volume $(\pi d^3/6)$ varies considerably, ranging between 5.2×10^{-4} and 1.8×10^{-6} cm^3 for the data shown. Hence, when the resuspended volume is made dimensionless using the particle volume the trend is reversed, and the number of resuspended particles is observed to decrease as d is increased.

It should be noted, however, that secondary effects do contribute to the value of ΔV measured. In particular, during the period of resuspension, the resuspended material caught in the field of view of the camera causes interference in the images used to calculate each displacement field; this effect produces an overestimate of V_d in the affected regions. The severity of the interference is dependent upon the concentration of the particles brought into suspension. That is, the interference is negligible in comparison to inherent noise when θ/θ_c is close to unity (at low concentrations). However, for the highest values of θ/θ_c considered, we expect this interference to be significant. Also, an overestimate of V_d will be caused by the change in packing density of the displaced sediment. In particular, we expect the regions of the sediment layer consisting of particles that have been displaced by the impact (or have resettled after suspension) to form with a lower packing density than that of the original layer formed using the scraping method (outlined in Sec. II). However, in our experiments, these effects were insignificant in comparison to noise levels associated with the light attenuation method (with $\Delta V\approx 0$ in all final-state crater profiles) and so could not be quantified.

Figure 14 also shows the initial sedimentation period of the resuspended volume, evident as the gradual decrease in ΔV observed for $(t-t_0)/\tau\gtrsim 2$ (the period during which the vortex structure breaks down). The two impacts shown in Figs. 7 and 8 (performed under the same conditions as the two experiments shown in Fig. 10) were found to have respective sedimentation periods of 1.2 and 0.5 s. For these impacts, the turbulent motions resulting from the breakdown

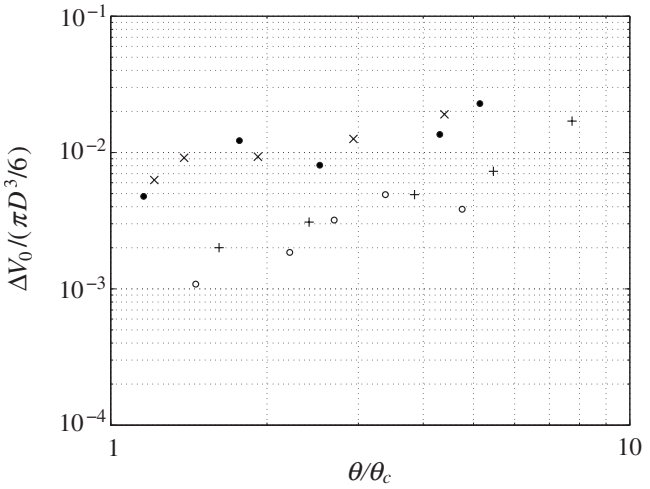

FIG. 15. The maximum volume difference ΔV_0 (made dimensionless using $\pi D^3/6$) plotted against θ/θ_c for a range of impact conditions. The different symbols correspond to particle types B (○, $d=150$ μm), D (+, $d=350$ μm), F (×, $d=700$ μm), and G (●, $d=1000$ μm), each having relative density $\gamma=2.5$.

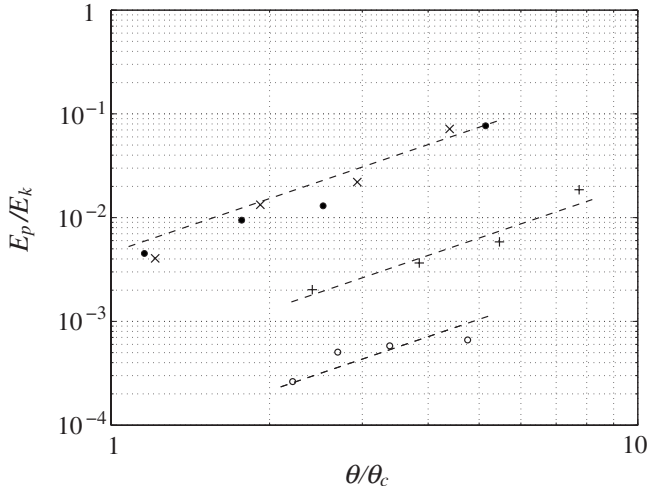

FIG. 16. Measured values of E_p/E_k plotted against θ/θ_c for a range of particle types. The different symbols correspond to particle types B (○, $d=150$ μm), D (+, $d=350$ μm), F (×, $d=700$ μm), and G (●, $d=1000$ μm), each having relative density $\gamma=2.5$.

of the vortex structure appear to have little effect on the period of sedimentation, which are approximately equal to the respective quiescent settling timescale, $D/2w_s$ (where $D/2$ represents the height to which the particles are resuspended above the layer). In general, the sedimentation period was found to increase with Re, when the intensity of the turbulence generated was sufficient to maintain particles in suspension for longer.

The efficiency with which the vortex ring erodes (or deforms) the sediment layer can be examined by comparing the quantity

$$E_p = 2\pi(\gamma-1)\rho g \int_0^\infty h^2(r,t_m) r\, dr \tag{6}$$

with the kinetic energy of the vortex ring, which, during the period of steady propagation, is proportional to $E_k=\rho D^3 U^2$ (assuming that the ring has a spherical form). Here, t_m is used to denote the time at which the maximum (vertical) penetration of the vortex ring into the bedform is first observed. That is, E_k represents the translational kinetic energy of the vortex ring (not the energy associated with the rotational motion), so that E_p may be interpreted as an estimate for the potential energy of the deformed particle layer at the point of maximum erosion. (We could improve this estimate by including an estimate for the packing density of the bed, but this is unknown and does not affect the essence of this discussion.) Figure 16 shows measured values of E_p/E_k plotted for a range of impact conditions, θ/θ_c, with each symbol representing a different sediment type, all with $\gamma=2.5$ (see caption for details). Clearly, E_p/E_k is dependent on d (as already demonstrated by Fig. 11), being comparable for the largest two particle types ($d=700$ and 1000 μm) but decreasing significantly as the sediment is made finer. For each of the sediment types shown, the monotonic increase in E_p/E_k with θ/θ_c (over the range of θ/θ_c considered) is well described by the relationship

$$E_p/E_k \sim (\theta/\theta_c)^\alpha. \tag{7}$$

Fitting Eq. (7) to each set of data returned an average value of $\alpha=1.54$ with a standard deviation of ± 0.18 (calculated from the fitted α values). The broken lines included in Fig. 16 show curves fitted to the data with $\alpha=3/2$. It should be noted, however, that limitations of the light attenuation method, associated with interference caused by high concentrations of resuspended material, meant that the range of impact conditions considered here was restricted to $1<\theta/\theta_c<10$. Moreover, at the higher values of θ/θ_c considered, the collapse of the axial region (due to destabilization) is likely to have a significant effect.

IV. SUMMARY AND FINAL REMARKS

The experiments presented here examine the resuspension and erosion of particles induced by a vortex ring impacting with a sediment layer. A selection of near-spherical sediments were considered, with diameters between 90 and 1600 μm and relative density ranging from 1.2 to 7. In all cases, the bedform was scraped flat and horizontal prior to impact, with each vortex ring aligned to approach the layer vertically in an otherwise quiescent fluid. The results are examined in terms of the dimensionless Shields parameter, $\theta=U^2/(\gamma-1)gd$, defined using the vortex propagation speed U. Interest was focused upon impacts at and above the critical conditions for resuspension ($\theta/\theta_c \geq 1$).

Measurements of fluid velocity in the near-bed region were used to analyze the critical conditions for resuspension. In particular, the critical Shields parameter, θ_c, was examined as a function of particle Reynolds number Re_p and dimensionless particle size d/δ. For $Re_p \geq 8$ ($d/\delta \geq 15$), θ_c was found to be approximately constant and within the range $1 \leq \theta_c \leq 2$. As the sediment size was made finer (with $Re_p<8$, $d<150$ μm), the effects of viscous damping become significant, resulting in a monotonic increase in θ_c with decreasing d/δ. That is, when the particle size is comparable with δ, viscous stresses act to significantly reduce the hydro-

dynamic lift and drag forces induced by the vortex flow field on the near-surface sediment grains. These observations are consistent with the "hydrodynamic roughness" limit (i.e., $d=200$ μm) suggested by previous researchers.[32] In this range, the data are consistent with the $\theta_c \sim Re_p^{-1/2}$ scaling corresponding to the $Re_p \ll 1$ limit.

Observations of the sediment trajectories during the interaction show the individual grains to be predominantly displaced and resuspended from a region below the (circular) vortex core. The circular mound of displaced material that forms just beyond the instantaneous ring radius indicates that the particles are displaced primarily by the radial velocity component. The azimuthal velocity, arising due to the wavelike instability within the ring core, is of secondary significance, giving rise to asymmetric small-scale scarring features on the crater surface. Near-surface particles are resuspended by a combination of hydrodynamic lift and interparticle collisions; the particles then become entrained within the outer streamlines of the vortex and rapidly advected around the ring perimeter. After passing below the ring core, the resuspended grains are subject to a nonzero component of vertical velocity which acts to propel them away from the bed surface, forming the characteristic particle splash. Observations showed that the splash feature was initially observed at $(t-t_0)/\tau \approx 1$ and at $r/D \approx 0.6-0.7$. Resuspended material was also seen to be entrained within and advected around the secondary vortex ring ejected from the boundary layer during the interaction.

Time-dependent measurements of bedform deformation show the crater profile to be self-similar during the impact period and for a range of impact conditions, except for the more energetic impacts $(\theta/\theta_c > 5.5)$ and larger sediment types $(d > 600$ μm). Loss of similarity occurs when the vortex ring penetrates sufficiently far into the sediment layer for the crater slope to approach the repose limit, leading to slope destabilization. Around the axial stagnation point the unstable crater slope is unable to support the (normal) force induced by the stagnation pressure, which leads to local collapse of the crater structure in this region at smaller slopes than can be maintained in quiescent conditions. Conversely, the outer sidewall of the crater, which likewise approaches the repose limit, is not subjected to this stagnation pressure and so no significant premature collapse is observed. Even for the most energetic impacts considered, the crater profiles were not observed to approach the repose limit for sediment sizes less that 500 μm.

The erosion efficiency was examined by comparing the potential energy associated with the deformed crater profile, E_p (at the point of maximum penetration), to the translational kinetic energy (prior to the impact) of the vortex ring, E_k. Over the range of impact conditions considered, the data for a given particle size are well described by an empirical relationship of the form $E_p/E_k = k(\theta/\theta_c)^{\alpha}$. Fitted values of k ranged between 10^{-2} and 10^{-5}, being strongly dependent on and decreasing with d; α, however, was found to be essentially independent of d, with $\alpha \approx 3/2$.

The observations and measurements presented herein indicate how coherent vortex structures propagating toward, and interacting with, a flow boundary play an important role in the resuspension and transport of sediment. During impact, the intense vorticle flow establishes local regions of high-speed fluid adjacent to the boundary which act to thin (or disrupt[13]) the inner viscous sublayer, thereby exposing the near-surface sediment grains in this region to greater hydrodynamic drag and lift forces. If the necessary conditions are satisfied, the sediment grains may be displaced or resuspended. Although this specific mechanism was suggested previously by Sutherland,[13] this article provides a detailed set of visual and quantitative data to confirm the basis of this hypothesis. Moreover, this study identifies the erosion, deposition and resuspension mechanisms associated with this phenomenon.

Note that the results and conclusions presented here are valid for the range of sediment types and impact conditions used in this study. For example, effects due to bed slope were not considered, with the sediment range restricted to micron-sized, cohesionless particles. A detailed study, using both vortex rings and grid-generated turbulence, is currently being undertaken to investigate these conditions.

ACKNOWLEDGMENTS

We would like to express our gratitude to The Royal Society (Grant No. RC0655) and the Engineering and Physical Sciences Research Council (EPSRC Grant No. GR/R25620/01) for financial support. N.B. was supported by the EPSRC (Mathematics CASE Award No. 014/004), AstraZeneca and Syngenta. The authors gratefully acknowledge Brian Dean, John Milton, David Page-Croft, and Trevor Parkin for technical support.

[1] A. Shields, "Anwendung der Ahnlichkeitsmechanik und der turbulenzforschung auf die geschiebebewegung," Preussiche Versuchsansalt für Wasserbrau und Schiftbrau **26**, 26 (1936).
[2] C. M. White, "The equilibrium of grains in the bed of a stream," Proc. R. Soc. London, Ser. A **174**, 322 (1940).
[3] R. A. Bagnold, "The movement of a cohesionless granular bed by fluid flow over it," Br. J. Appl. Phys. **2**, 29 (1951).
[4] J. R. D. Francis, "Experiments on the motion of solitary grains along the bed of a water-stream," Proc. R. Soc. London, Ser. A **332**, 443 (1973).
[5] B. M. Sumer and B. Oguz, "Particle motions near the bottom in turbulent flow in an open channel," J. Fluid Mech. **86**, 109 (1978).
[6] B. M. Sumer and R. Deigaard, "Particle motions near the bottom in turbulent flow in an open channel. Part 2," J. Fluid Mech. **109**, 311 (1981).
[7] D. Kaftori, G. Hetsroni, and S. Banerjee, "Particle behaviour in the turbulent boundary layer. I. Motion, deposition and entrainment," Phys. Fluids **7**, 1095 (1995).
[8] D. Kaftori, G. Hetsroni, and S. Banerjee, "Particle behaviour in the turbulent boundary layer. II. Velocity and distribution profiles," Phys. Fluids **7**, 1107 (1995).
[9] Y. Ninto and M. H. Garcia, "Experiments on particle-turbulence interactions in the near-wall region of an open channel flow: implications for sediment transport," J. Fluid Mech. **326**, 285 (1996).
[10] C. Ancey, F. Bigillon, P. Frey, J. Lanier, and R. Ducret, "Saltating motion of a bead in a rapid water stream," Phys. Rev. E **66**, 036306 (2002).
[11] C. Ancey, F. Bigillon, P. Frey, J. Lanier, and R. Ducret, "Rolling motion of a bead in a rapid water stream," Phys. Rev. E **67**, 011303 (2003).
[12] R. G. Jackson, "Sedimentological and fluid-dynamical implications of the turbulent bursting phenomenon in geophysical flows," J. Fluid Mech. **77**, 531 (1976).
[13] A. J. Sutherland, "Proposed mechanism for sediment entrainment by turbulent flows," J. Geophys. Res. **72**, 6183, DOI: 10.1029/JZ072i024p06183 (1967).
[14] T. Maxworthy, "The structure and stability of vortex rings," J. Fluid Mech. **51**, 15 (1972).
[15] P. F. Linden, "The interaction of a vortex ring with a sharp density inter-

face: a model for turbulent entrainment," J. Fluid Mech. **60**, 467 (1973).
[16]W. J. A. Dahm, C. M. Scheil, and G. Tryggvason, "Dynamics of vortex interaction with a density interface," J. Fluid Mech. **205**, 1 (1989).
[17]J. D. A. Walker, C. R. Smith, A. W. Cerra, and T. L. Doligalski, "The Impact of a vortex ring on a wall," J. Fluid Mech. **181**, 99 (1987).
[18]P. Orlandi and R. Verzicco, "Vortex rings impinging on walls: axisymmetric and three-dimensional simulations," J. Fluid Mech. **256**, 615 (1993).
[19]J. D. Swearingen, J. D. Crouch, and R. A. Handler, "Dynamics and stability of a vortex ring impacting a solid boundary," J. Fluid Mech. **297**, 1 (1995).
[20]H. E. Huppert, J. S. Turner, and M. A. Hallworth, "Sedimentation and entrainment in dense layers of suspended particles stirred by an oscillating-grid," J. Fluid Mech. **289**, 263 (1995).
[21]J. J. Orlins and J. S. Gulliver, "Turbulence quantification and sediment resuspension in an oscillating grid chamber," Exp. Fluids **34**, 662 (2003).
[22]J. Colomer and H. J. S. Fernando, "Resuspension of sediments by multiple jets," J. Hydrol. Eng. **125**, 765 (1999).
[23]R. J. Munro, S. B. Dalziel, and H. Jehan, "A pattern matching technique for measuring sediment displacement levels," Exp. Fluids **37**, 399 (2004).
[24]R. J. Munro and S. B. Dalziel, "Attenuation technique for measuring sediment displacement levels," Exp. Fluids **39**, 602 (2005).
[25]P. G. Saffman, "On the formation of vortex rings," Stud. Appl. Math. **54**, 371 (1975).
[26]T. Maxworthy, "Some experimental studies of vortex rings," J. Fluid Mech. **81**, 465 (1977).
[27]A. Glezer, "The formation of vortex rings," Phys. Fluids **31**, 3532 (1988).
[28]J. J. Allen and B. Auvity, "Interaction of a vortex ring with a piston vortex," J. Fluid Mech. **465**, 353 (2002).
[29]N. Didden, "Formation of vortex rings—rolling-up and production of circulation," Z. Angew. Math. Phys. **30**, 101 (1979).
[30]As of October 2008, available at Dalziel Research Partners, 142 Cottenham Road, Histon, Cambridge CB24 9ET, UK.
[31]M. Phillips, "A force balance model for particle entrainment into a fluid stream," J. Phys. D: Appl. Phys. **13**, 221 (1980).
[32]S. J. White, "Plane bed thresholds for fine grained sediments," Nature (London) **228**, 152 (1970).
[33]I. Eames and S. B. Dalziel, "Dust resuspension by the flow around an impacting sphere," J. Fluid Mech. **403**, 305 (2000).
[34]W. R. Brownlie, "Flow depth in sand-bed channels," J. Hydraul. Eng. **109**, 959 (1983).
[35]S. E. Widnall and J. P. Sullivan, "On the stability of vortex rings," Proc. R. Soc. London, Ser. A **332**, 335 (1973).